Int. J. Electrochem. Sci., 13 **(2018)** 5667 – 5680, doi: 10.20964/2018.06.18

International Journal of
ELECTROCHEMICAL
SCIENCE
www.electrochemsci.org

One-step Facile Synthesis of Hierarchically Porous Nitrogen-Doped SnO_2 Nanoparticles with Ultrahigh Surface Area for Enhanced Lithium Storage Performance

Xiangfeng Guan[*], *Peihui Luo, Xiaoyan Li, Yunlong Yu, Dagui Chen*[*], *Lili Zhang*

College of Electronics and Information Science & Organic Optoelectronics Engineering Research Center of Fujian's Universities, Fujian Jiangxia University, Fuzhou, Fujian 350108, P.R. China
[*]E-mail: xfguan@fjjxu.edu.cn, dgchen@fjjxu.edu.cn

Received: 26 January 2018 / *Accepted:* 16 March 2018 / *Published:* 10 May 2018

In this work, one-step facile synthetic method was developed to obtain hierarchically porous nitrogen(N)-doped SnO_2 nanoparticles that exhibit enhanced lithium storage performance with a high discharge capacity of 590 mAh g^{-1} after 50 times cycles. The investigation by X-ray diffraction (XRD) and transmission electron microscopy (TEM) show that the crystal size of N-doped SnO_2 nanoparticles was controlled to 2-3 nm. Moreover, the N_2 adsorption–desorption results suggest micropores (1.2 nm) and mesopores (< 5 nm) characters for N-doped SnO_2 nanoparticles with ultrahigh specific areas (212.7 m^2 g^{-1}). The doping concentration of N tested by elemental analyzer was found to be 2.7 at%. X-ray photoelectron spectroscopy (XPS) and Electron paramagnetic resonance (EPR) measurements further confirm that N doping results in the increase of the concentration of oxygen vacancy defects. The enhanced lithium storage performance of N-doped SnO_2 nanoparticles can be ascribed to ultrafine particle size, ultrahigh specific surface area, the high concentration of oxygen vacancy defects, as well as the unique hierarchically porous structure. All the results indicated that the N-doped SnO_2 nanoparticles have a great potential for application as anodes for lithium ion batteries.

Keywords: One-step synthesis; Nitrogen-doped SnO_2; Micro-mesoporous; Lithium-ion batteries

1. INTRODUCTION

Lithium ion batteries (abbreviated as LIBs) have been intensively applied in fields of portable mobile electronic devices and electric vehicles, thanks to their high energy density and robust cycling performance [1]. The cathode and anode materials of LIBs are the host of lithium ion storage, which play a key role in the electrochemical performances of LIBs. Graphite is the most utilized anode material, which is however in face of two main problems, i.e., relatively low theoretical capacity (372 mAh g^{-1}) and Li plating at high current rates [2]. Among various alternative anode materials with high

capacity, tin oxide (SnO_2) have been widely investigated due to their low working voltage and high specific capacity (782 mAh g^{-1}) [3]. SnO_2 based LIBs have the advantages of low cost and high energy density, but their capacity decreases rapidly due to the huge volume changes during Li-ion insertion and de-insertion process, which could result in agglomeration and pulverization [4]. Therefore, seeking high-performance SnO_2 anode materials have been one of the hottest issues in relative research fields.

Up to date, several strategies have been adopted to improve the electrochemical performances of SnO_2 anode, which include reduction of the particle size of SnO_2 by nanostructuring [5], and substitution of metallic Sn with other elements [6-13], and preparations of SnO_2/carbon composites [14]. With regards to the substitution of metallic Sn with other elements, much effort have been devoted in metal cations such as Ni [6], Sb [7, 8], Al [9], Mo [10], In [11], as well as non-metal anion such as F [12], and N [13], which have confirmed that these dopants could improve the lithium storage properties by increasing the conductivity. Recently, it is reported that the intrinsic conductivity of metal oxides could be greatly improved by N doping [15] due to the production of oxygen vacancy defects [16]. In bulk N-doped SnO_2, significantly enhanced conductivities are also observed [17]. Wang et al. [13] developed an ingenious laser-assisted pyrolysis method by using NH_3 gas as nitrogen sources. The obtained N-doped SnO_2 nanoparticles exhibited outstanding lithium storage properties. Unfortunately, most of methods involve sophisticated step, expensive facilities, and high-temperature calcinations. Therefore, from the viewpoint of facilitating operation simplicity and the wide application of the LIBs, one-step facile synthesis of N-doped SnO_2 nanoparticles electrode with enhanced electrochemical performance is highly desirable.

In this work, we have successfully developed one-step facile approach to obtain porous N-doped SnO_2 nanoparticles. The crystal size of ultrafine N-doped SnO_2 was controlled to 2-3 nm. The N-doped SnO_2 nanoparticle features highly porous structure with micro/mesoporous pores well below 5 nm, enabling an ultrahigh surface area of 212.7 $m^2 \cdot g^{-1}$ which represents one of the highest values reported to date on SnO_2 nanostructures. Due to the unique micro/mesoporous structure, small grain size, and the rich oxygen vacancy produced by nitrogen doping, the N-doped SnO_2 nanoparticles electrode show enhanced lithium storage properties. We believe our findings will provide new insights on the doping of nanostructures, which holds potential for the development of high-performance electrodes for LIBs.

2. EXPERIMENTAL

2.1 Materials

Analytical grade chemicals of stannic chloride pentahydrate ($SnCl_4 \cdot 5H_2O$) and hexamethylenetetramine (HMT), ethanol were used as the starting materials without further purification. $SnCl_4 \cdot 5H_2O$ and HMT was used as tin and nitrogen sources, respectively.

2.2 Synthesis of pristine SnO_2 and N-doped SnO_2 (N-SnO_2)

In a typical synthesis procedure of nitrogen-doped SnO_2, a given quantity of $SnCl_4$•$5H_2O$ was added to 32 mL of ethanol to form a transparent clear solution. Then, a desired amount of HMT was added to the above solution. The molar ratio of Sn^{4+}/HMT was 1:3. The mixture was vigorously agitated for 30 min. Then the suspension was transferred to a 45 mL hydrothermal bomb, which was heated at 180 ^oC for 24 h. The bomb was cooled naturally to room temperature after heat treatment. The brown powder was filtered and washed with excess water and absolute alcohol, and finally dried in air at 80 ^oC overnight. For the synthesis of pristine SnO_2, the synthesis conditions are unchanged except for the absence of HMT.

2.3 Materials characterization

The phase structures of the samples were characterized via x-ray diffraction (XRD). The morphologies and microstructures were determined using field emission scanning electron microscopy (FESEM) and transmission electron microscopy (TEM). Valence states and chemical compositions of the samples were determined by X-ray photoelectron spectroscopy (XPS). The nitrogen content was determined by the elemental analyzer. The defects of the samples were characterized via Electron paramagnetic resonance (EPR). The band-gap energies of the samples were investigated using UV–visible diffuse reflectance spectroscopy (UV-vis DRS). The pore size distribution and specific surface area of the samples were derived using the Density Functional Theory (DFT) model and the multipoint Braunauer-Emmett-Teller (BET) method, respectively.

2.4 Electrochemical characterization

The pristine SnO_2 and N-SnO_2 samples were used as anode active materials for LIBs. The anode materials were prepared by mixing the SnO_2 active materials, acetylene black, and carboxymethylcellulose at weight ratios of 70:20:10, respectively, using deionized water as a solvent. The resultant slurry was coated onto copper foil and dried at 120 ^oC under vacuum overnight to remove residual water. The dried anode electrode was then cut into desired size according to the diameter of CR2025 coin-type cell. The coin-type cells were assembled in an argon-filled glove box. The lithium foil and polypropylene film were used as counter electrode and separator, respectively. The electrolyte was 1M $LiPF_6$ in ethylene carbonate (EC) : ethyl methyl carbonate (EMC) : dimethyl carbonate (DMC) (1:1:1 in volume). The assembled cells were galvanostatically charged and discharged at 28 ^oC using a NEWARE battery tester within a voltage window between 0.01 and 3.0 V. The cyclic voltammetry (CV) was measure on an electrochemical workstation (CHI660E) with a scan rate of 0.1 mV s^{-1}.

3. RESULTS AND DISCUSSION

3.1 Designed synthesis of N-SnO_2

In this work, we develop a new synthetic strategy for hierarchically porous N-SnO_2 nanoparticles, as shown in Figure 1. $SnCl_4$•$5H_2O$ was used as Sn-source, which was commonly used in the synthesis of SnO_2 in solvothermal method. Ethanol was chosen as the reaction solvent to slow down the hydrolysis of $SnCl_4$, considering the trace water in $SnCl_4$•$5H_2O$ could provide the water necessary for hydrolysis reaction. Furthermore, the low solubility of SnO_2 in ethanol will result in the more slowly crystal growth rate [18]. HMT is employed as the N-source for the doping. It is regarded that HMT is a good alternative for N-doping due to its high solubility in water and polar organic solvents.

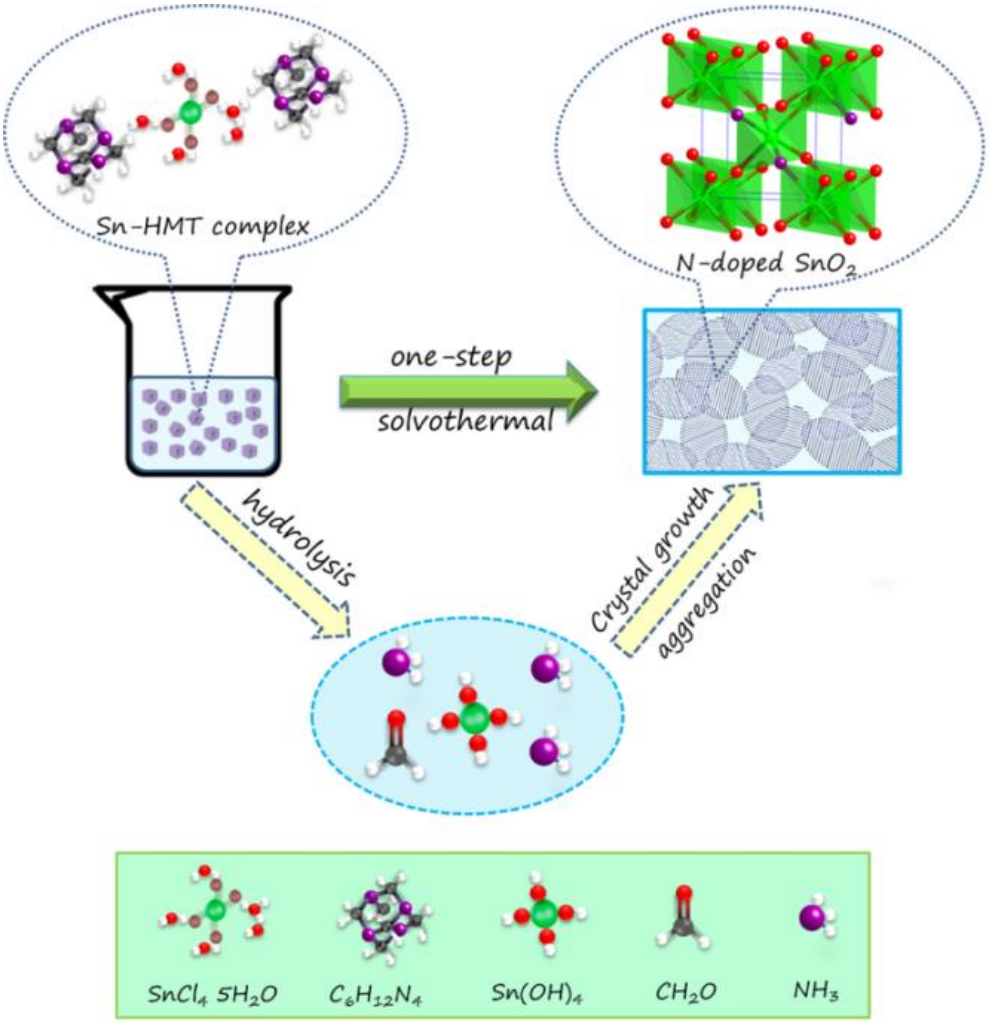

Figure 1. Scheme that illustrates the direct synthesis route to N-doped SnO_2 (N-SnO_2).

Also the cage-like structure will facilitate the coordination of N to the surface Sn atom of SnO_2 [19]. When heated, HMT can react with water and the released NH_3 which will promote nitrogen

doping in SnO_2 [20]. During one-step solvothermal process, the hydrolysis of $SnCl_4 \cdot 5H_2O$ and HMT proceed simultaneously. Tiny crystalline nuclei that formed in the supersaturated solution will fast grow into primary nanoparticles, which will further aggregated spontaneously with minimizing interfacial energies. The N atoms of the ligand will be adsorbed on the surface of the primary particles and thus be included in between the crystal face during the aggregation, impeding further crystal growth of SnO_2. Through control the hydrolysis rate as well as the lattice shrinkage effect of nitrogen doping, the crystal size of N-SnO_2 can be controlled to be 2-3 nm, enabling the construction of micro/mesoporous pores well below 5 nm. Thus, microporous/mesoporous N-SnO_2 nanoparticles with ultrahigh specific surface area were obtained.

3.2. Morphology and structural characterization

The photo of as-prepared pristine SnO_2 and N-SnO_2 samples are shown in Figure 2a. Unlike standard white pristine SnO_2, N-SnO_2 powders are brown, which indicates that nitrogen element has been successfully doped in SnO_2. The phenomenon of colour change caused by nitrogen doping was also seen in nitrogen-doped TiO_2 [21]. Figure 2b shows the XRD patterns of as-prepared pristine SnO_2 and N-SnO_2. All diffraction peaks of the pristine SnO_2 sample can be well indexed to the standard diffraction data for SnO_2 with a rutile structure (PDF. No. 41-1445). No other phase is detected, which reveals the purity of the products. Comparatively, the diffraction peaks of the N-SnO_2 sample are apparently widened, indicating small crystallite size.

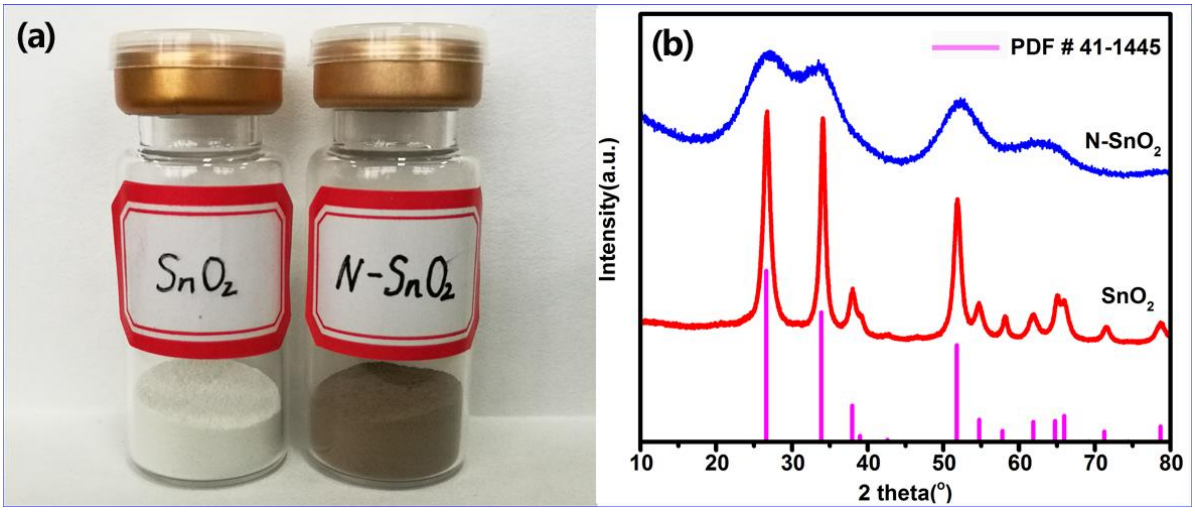

Figure 2. Pristine SnO_2 versus N-SnO_2. (a) SnO_2 powder (left) and N-SnO_2 powder (right); (b) XRD patterns of pristine SnO_2 and N-SnO_2.

The morphologies and microstructures are investigated by SEM, TEM, and high-resolution TEM (HRTEM). The SEM image (Figure 3a) shows that the pristine SnO_2 sample was composed of homogenously distributed particles of sizes between 40 and 60 nm. The TEM image (Figure 3b) reveals that these particles are the aggregates of spacious nanocrystallites of 10-15 nm in diameter. The

selected-area electron diffraction (SAED) pattern (inset of Figure 3b) demonstrates distinct bright diffraction spots of SnO_2. The HRTEM images (Figure 3c) reveal well-resolved lattice lines with 0.33 nm lattice spacing, which is corresponding to the (110) plane of SnO_2. Comparatively, the SEM image of N-SnO_2 (Figure 3d) shows the presence of large irregular particles of sizes between 300 nm and 1 μm. The TEM image (Figure 3e) demonstrates that the large irregular particles are composed of many tiny nanocrystallites. The SAED pattern (inset of Figure 3e) shows the existence of diffuse diffraction rings instead of distinct bright spots, indicating highly polycrystalline nature. The HRTEM image (Figure 3f) further shows that the tiny nanocrystallites are mainly 2-3 nm in diameter, close to the exciton Bohr radius of 2.7 nm for SnO_2 [22]. The apparent decrease in size of the N-SnO_2 sample is possible ascribed to the introduction of nitrogen atoms into SnO_2, which could suppress the formation of long-range order in SnO_2 lattice [23]. The interlayer spacings of 0.26 and 0.33 nm of the nanocrystallites are observed, which correspond to the (101) and (110) planes for tetragonal phase SnO_2, respectively. Additionally, small pores are observed in the pristine SnO_2 and N-SnO_2, as shown in Figure 3c and 3f.

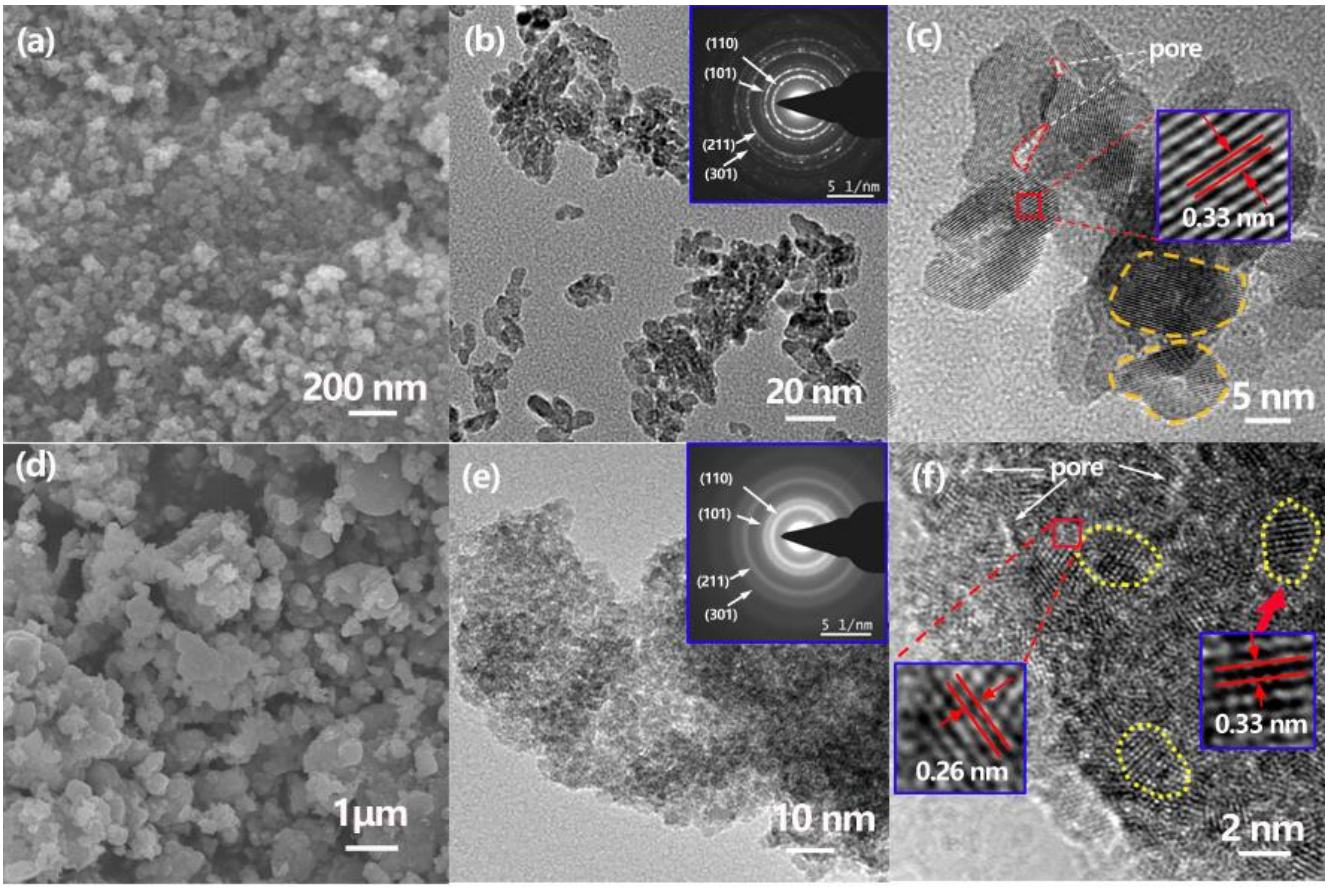

Figure 3. (a) SEM, (b) TEM, (c) HTEM images of pristine SnO_2 and (d) SEM, (e) TEM, (f) HTEM images of N-SnO_2. The insets display the corresponding SAED patterns and interlayer spacing.

XPS measurements were carried out to obtain detailed information on the surface composition and redox states of Sn and N in the pristine SnO_2 and N-SnO_2 samples. The general survey scan of the entire spectrum was calibrated with a C 1s standard (284.8 eV) before analysis. Figure 4 presents the

emission spectra of Sn 3d, N 1s, and O 1s peaks in all samples. The Sn 3d spectra of pristine SnO_2 (Figure 4a) show the standard Sn $3d_{5/2}$ and Sn $3d_{3/2}$ peaks of rutile SnO_2 at 486.8 and 495.2 eV, respectively, thus implying that Sn exists only in the 4+ state [24]. Their difference of 8.4 eV, being the binding energy of Sn's 3d electron, also agrees with that in the standard database [16]. For N-SnO_2 sample, both binding energy of Sn $3d_{5/2}$ and $3d_{3/2}$ show a slight shift (~ 0.2 eV) to lower energy, indicating the doping with nitrogen and formation of oxygen vacancies.

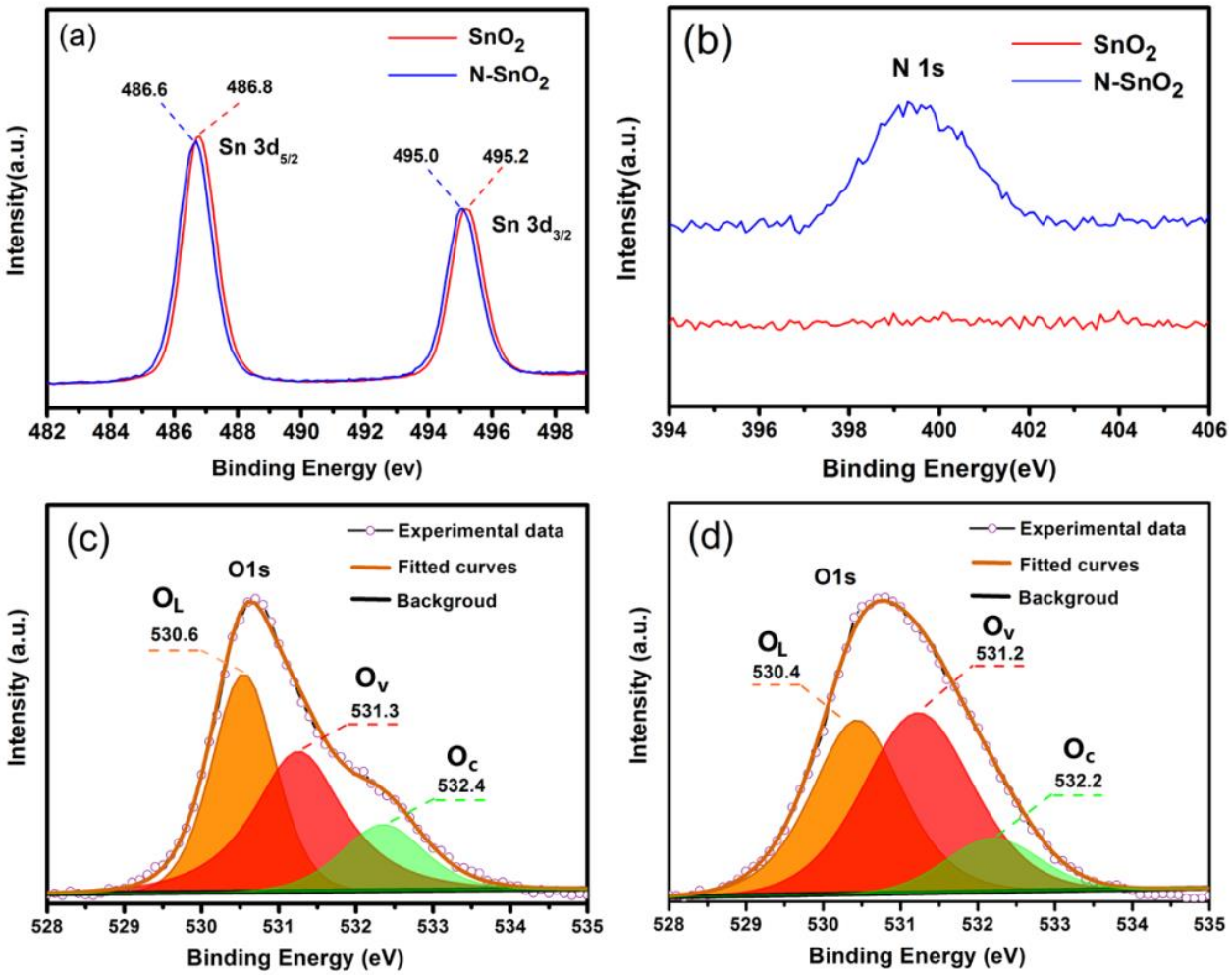

Figure 4. Binding energy spectra of as-prepared samples: (a) Sn, 3d (b) N 1s of the pristine SnO_2 and N-SnO_2 samples, (c) O 1s spectrum of pristine SnO_2, and (d) O 1s spectrum of N-SnO_2.

The variation of core binding energy of Sn $3d_{5/2}$ and $3d_{3/2}$ could be attributed to that a more negative N^{3-} compared with O^{2-} that results in shifting of 3d orbital energy level due to higher coulombic potential [25]. Figure 4b shows the N 1s spectra of the samples. It can be found that there is an intense N 1s peak around 399.5 eV in the N-SnO_2 sample, which confirmed the existence of nitrogen atoms in the N-SnO_2 sample. The nitrogen compositions for the sample were tested by elemental analyzer, which is found to be 2.7 at%. Figure 4c shows the O 1s spectra of the pristine SnO_2 sample. The asymmetric O 1 s peaks could be decomposed into three contributions of 530.6, 531.3, and 532.4 eV, which can be attributed to lattice oxygen (O_L), oxygen vacancies (O_V), and

chemisorbed oxygen species (O_C), respectively [26]. However, the O 1 s peaks in the N-SnO_2 sample were relatively symmetric. It could also be deconvoluted into three curves at 530.4, 531.2, and 532.2 eV. It shows a significant increase of the peak area of O_V, suggesting an increase of O_V contents in SnO_2 by nitrogen doping.

EPR was used to evaluate the defect state of the samples. Figure 5a shows the EPR signals for the pristine SnO_2 and N-SnO_2 samples. The EPR spectrum of pristine SnO_2 does not show any signal. In contrast, that of N-SnO_2 sample shows a unique intense signal with g value ~2.00 confirming the presence of oxygen vacancies. The band-gap energies of the samples are determined by using UV-vis DRS. As shown in Figure 5b, the spectrum of N-SnO_2 sample shows obvious adsorption in the visible-light region which is in accordance with the brown look of the in appearance of N-SnO_2 powder. The band gap energy can be obtained by fitting the optical transition at the absorbance edge with the equation $\alpha = A (E - E_g)^n$, where n = 0.5 represents a direct transition and n = 2 represents an indirect transition. The fitting results of the spectra of the pristine and N-SnO_2 indicates that both are direct type semiconductor. The values of E_g for the pristine SnO_2 and N-SnO_2 samples were 3.8 and 3.7 eV, respectively, which are higher than that of 3.6 eV for bulk SnO_2 [27]. It has been reported that the decrease in particle size could lead to the increase of band-gap energy, thus the particle size effect can be attributed to the increased band-gap energy of the pristine SnO_2 and N-SnO_2 samples. It is worth noting that the particle sizes of the N-SnO_2 sample are much smaller than that of the pristine SnO_2, while its band-gap energy is smaller. For the N-SnO_2 sample, the band structure is also relevant to doping effects aside from the particle size. It is well documented that the nitrogen doping could lead to a red shift of the absorption peak. It seems that the effect of nitrogen doping dominates the variation of E_g of the N-SnO_2 sample.

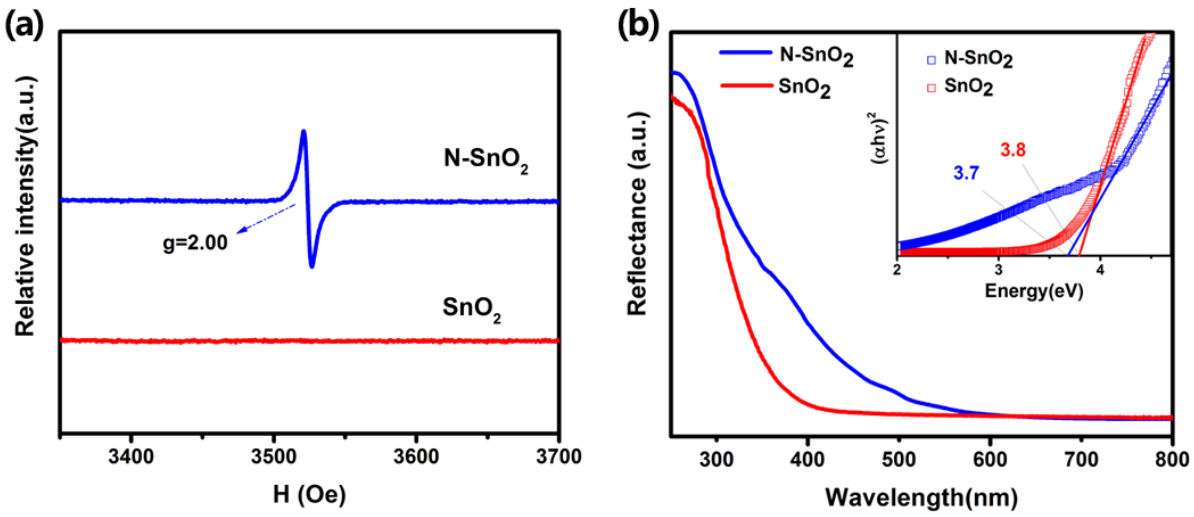

Figure 5. (a) EPR signals and (b) optical diffuse reflectance spectra of the pristine SnO_2 and N-SnO_2 samples. The inset shows the energy dependence of $(\alpha h\nu)^2$ for the samples.

The pore size distribution and BET surface area for the pristine SnO_2 and N-SnO_2 samples were investigated by N_2 adsorption/desorption analysis. From the pore size distribution curve in Figure 6a, the pristine SnO_2 sample exhibits mesopores (from 5 to 30 nm) and micropores (from 1 to 2 nm), with the mean pore diameter of ca. 1.3 nm. Comparatively, for N-SnO_2 sample, the mesopore sizes are mainly located in the range of 2-5 nm and the volume of micropores apparently increased, with the mean pore diameter decreasing to ca. 1.2 nm. Surprisingly, the BET specific surface area of the N-SnO_2 sample is 212.7 $m^2 \cdot g^{-1}$, which is more than two times of that for the pristine SnO_2 sample (97.1 $m^2 \cdot g^{-1}$). It is noticeable that such feature that possesses both high specific surface area (212.7 $m^2 \cdot g^{-1}$) and small mean pore size (1.2 nm) has been scarcely reported. Figure 6b shows the corresponding values of SnO_2 materials in previous literatures [28-44]. It suggests that the ultrahigh specific surface area and ultrasmall mean pore size in SnO_2 system can be achieved without using any surfactants/capping agent or entailing expensive facilities.

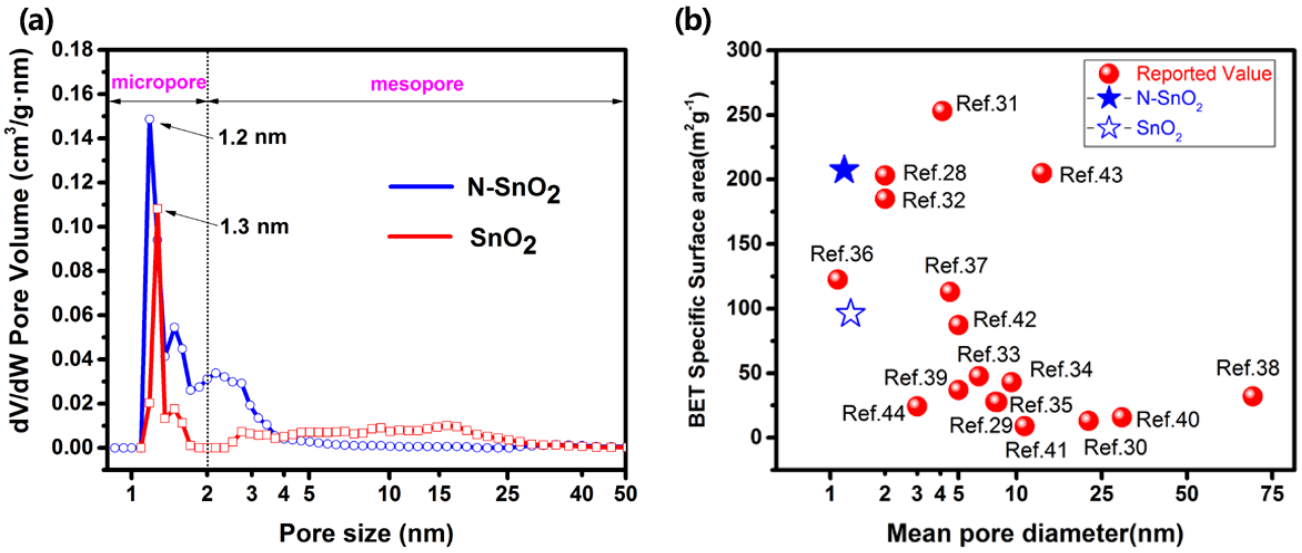

Figure 6. (a) Pore size distribution of the pristine SnO_2 and N-SnO_2 samples and (b) relative data comparison between this work and reported SnO_2-based materials. (BET specific surface area versus mean pore diameter)

3.3. Lithium storage properties

To study the lithium storage properties and related electrochemical reaction mechanism, the as-prepared SnO_2 samples were assembled to the coin-type cells and measured by CV and galvanostatical charge-discharge technique. The CV measurement was performed to study the electrochemical reaction mechanism during the Li-ion insertion and de-insertion process. Figure 7 shows the first five CV curves of the cells assembled from pristine SnO_2 and N-SnO_2 electrodes between 0.01 and 3 V at a scan rate of 0.1 mV s^{-1}. For pristine SnO_2 electrode (Figure 7a), there are two cathodic peaks and two anodic peaks observed during the first cycle. The cathodic peak around 0.79 V is associated with the formation of solid electrolyte interphase (SEI) layers and the conversion of SnO_2 to Sn and Li_2O [45]. Another cathodic peak located at 0.12 V is ascribed to the insertion of Li-ion into metallic Sn to form

Li_xSn alloy [46]. The anodic peak around 0.58 V can be ascribed to the de-insertion of Li-ion in Li_xSn alloy to form metallic Sn and another anodic peak located at 1.24 V corresponds to the formation of SnO_2 resulted from the oxidation of metallic Sn [47]. In the subsequent cycles, the cathodic peak around 0.79 V disappeared and a broad cathodic peak around 1.06 V was observed which can be ascribed to the conversion of SnO_2 to Sn and Li_2O. For N-SnO_2 electrode (Figure 7b), similar CV curve profile was observed. It is found that the intensity of cathodic peak at 0.12 V and anodic peak at 0.56 V are much stronger than that of pristine SnO_2 electrode, which can be ascribed to the improved electronic conductivity resulted from oxygen vacancy defects in N-SnO_2 electrode [16]. Additionally, the integral areas of N-SnO_2 electrode are larger than that of pristine SnO_2 electrode, indicating the enhanced electrochemical activity.

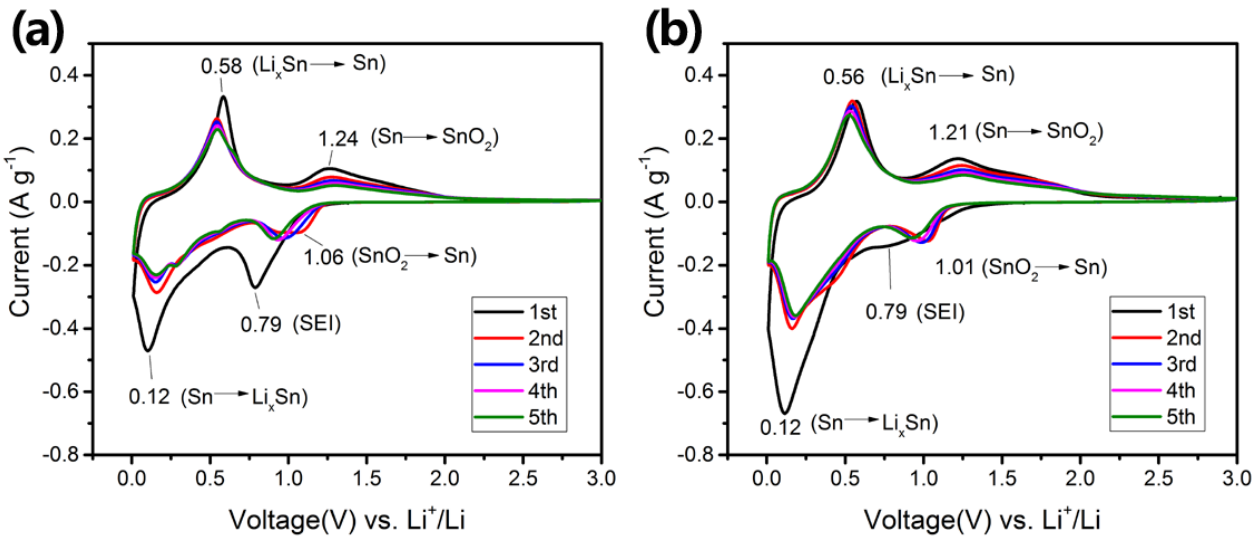

Figure 7. The first five CV curves of the cells assembled from (a) pristine SnO_2 and (b) N-SnO_2 electrodes between 0.01 and 3 V at a scan rate of 0.1 mV s^{-1}.

The lithium ion storage properties of pristine SnO_2 and N-SnO_2 electrodes were evaluated by galvanostatical charge-discharge technique at a current density of 0.1 A g^{-1}. Figure 8 shows the initial charge-discharge curve of pristine SnO_2 electrode and N-SnO_2 electrode. It can be seen that, for both sample electrodes, two slope regions can be observed in both discharge and charge process, which agrees with the CV results and previous reports [48]. The initial discharge capacities of pristine SnO_2 electrode and N-SnO_2 electrode are 1944 and 2348 mAh g^{-1}, respectively, which are much higher than the theoretical capacity of SnO_2 (782 mAh g^{-1}). It is well documented [49, 50] that the extra discharge capacity can be ascribed to the formation of SEI layer resulted from the decomposition of electrolyte, interfacial lithium storage, and porous structure that may trap more Li-ion. In addition, the initial charge capacities of pristine SnO_2 and N-SnO_2 electrode decreased to 915 and 1339 mAh g^{-1}, respectively.

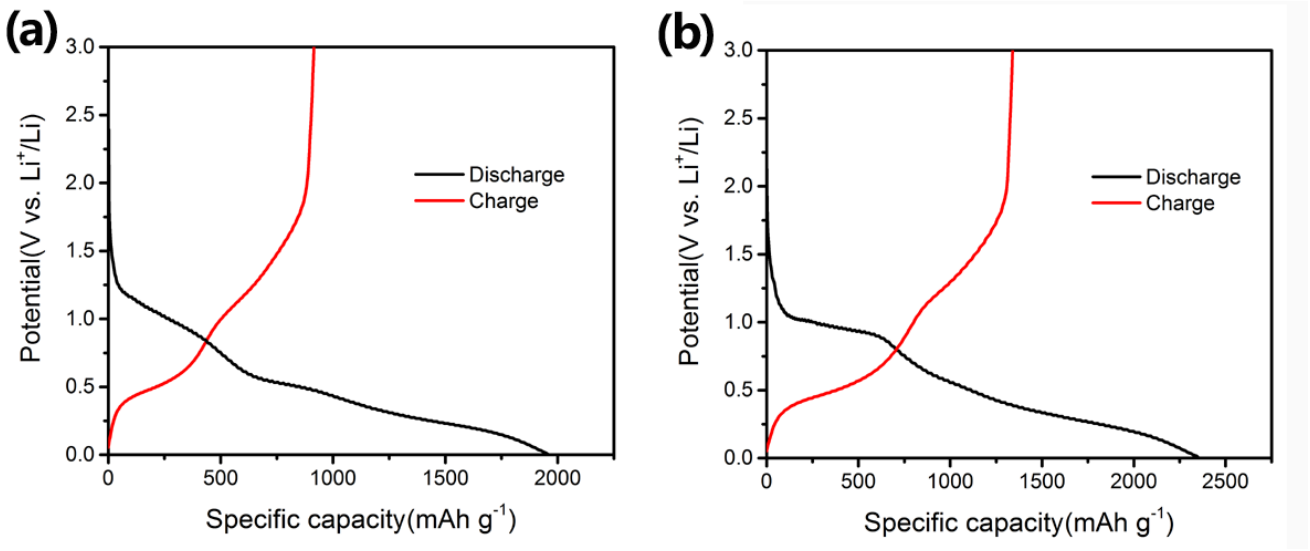

Figure 8. Galvanostatic charge-discharge curves of (a) pristine SnO_2 and (b) N-SnO_2 electrodes between 0.01 and 3 V at a current density of 0.1 A g^{-1}.

Figure 9 shows the cycling performance of pristine SnO_2 and N-SnO_2 electrodes at a current density of 0.1 A g^{-1}. It is seen that N-SnO_2 electrode exhibited better cycle performance than pristine SnO_2 electrode at the same current density. After 50 cycles, the reversible discharge capacity of pristine SnO_2 electrode rapidly decreased from 915 to 373 mAh g^{-1} (Figure 9a). Comparatively, N-SnO_2 electrode still delivered a reversible discharge capacity of 590 mAh g^{-1}, accompanied with a high Coulumbic efficiency of 96% (Figure 9b).

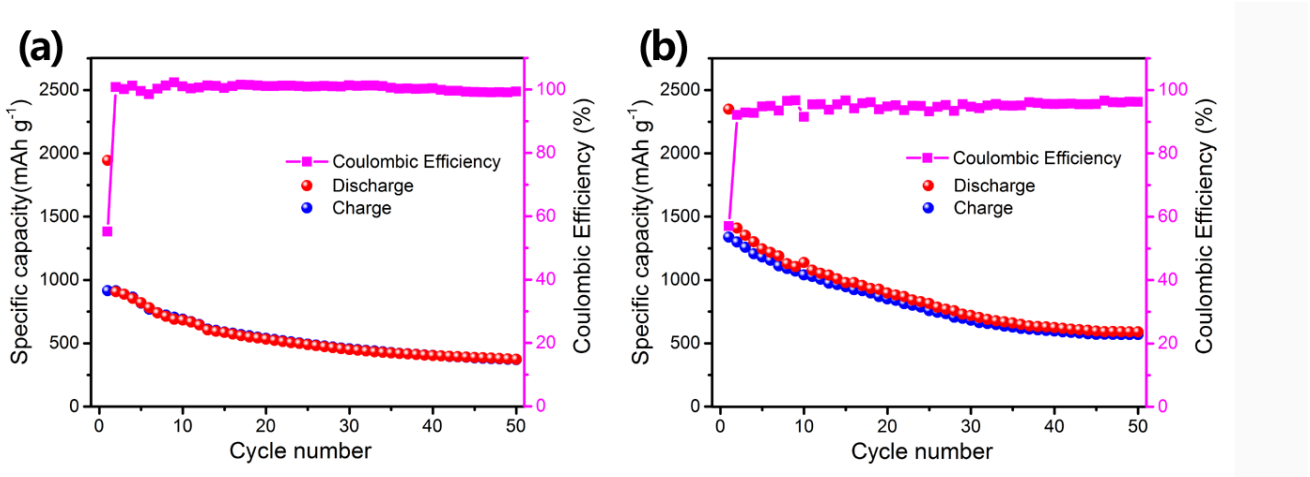

Figure 9. Cycling performance of (a) pristine SnO_2 and (b) N-SnO_2 electrodes at a current density of 0.1 A g^{-1}.

As can be seen in Table 1, the specific discharge capacitance of N-SnO_2 electrode after being cycled 50 times at the current density of 0.1 A g^{-1} is superior to that of Sb-doped SnO_2 microspheres, Al-doped SnO_2 hollow sphere, In-doped SnO_2 nanocrystallites, F-doped SnO_2 powder, SnO_2 nanosheet, and comparable with that of SnO_2/graphene based materials cycled at smaller current

densities that are more beneficial to obtain large capacity. The enhanced lithium storage properties of N-SnO_2 electrode can be ascribed to the following factors: (i) The ultrafine particle size and high specific area could provide more active sites for Li-ion insertion and de-insertion [51]. (ii) The microporous-mesoporous structure can facilitate the penetration of electrolyte and shorten transport path of electron and Li-ion [52]. (iii) The enhanced oxygen vacancy defects could improve the electric conductivity, which may contribute to improving the lithium-diffusivity for better electrochemical performance [53].

Table 1. Electrochemical performance of N-SnO_2 sample and previously reported SnO_2 based materials

Materials	Preparation method	Current density	Initial Capacitance ($mAh\ g^{-1}$)	Cycle number	Remaining capacitance ($mAh\ g^{-1}$)	References
Sb-doped SnO_2 microspheres	solvothermal	~0.157 A g^{-1}	1981	50	227	[7]
Al-doped SnO_2 hollow sphere	hydrothermal	~0.078 A g^{-1}	1821	50	~490	[9]
In-doped SnO_2 nanocrystallites	precipitation	0.5 mA cm^{-2}	1744	10	~500	[11]
F-doped SnO_2 powder	Sol-gel	0.025 A g^{-1}	1775	25	268	[12]
SnO_2 nanosheet	hydrothermal	~0.078 A g^{-1}	~1900	20	559	[54]
SnO_2/graphene	hydrothermal	0.05 A g^{-1}	2634	60	650	[55]
N-SnO_2 nanoparticles	solvothermal	0.1 A g^{-1}	2348	50	590	This work

4. CONCLUSIONS

In summary, the hierarchically porous N-doped SnO_2 nanoparticles were achieved by a direct solvothermal process using environmentally friendly and inexpensive Sn-source and N-source. The resultant 2-3 nm N-doped SnO_2 nanoparticles were featured as a highly porous structure with micro/mesoporous pores well below 5 nm, enabling an ultrahigh surface area of 212.7 $m^2\ g^{-1}$. When evaluated as anode material for LIBs, the prepared hierarchically porous N-doped SnO_2 nanoparticles

exhibited obviously enhance lithium storage properties, which delivered a high reversible discharge capacity of 590 mAh g^{-1} after 50 times cycles. The enhanced lithium storage performance of N-doped SnO_2 nanoparticles can be ascribed to ultrafine particle size, ultrahigh specific surface area, the high concentration of oxygen vacancy defects, as well as the unique hierarchically porous structure. The findings reported here could open a way for design the nitrogen-doped metal oxides. And we anticipate that the N-doped SnO_2 nanoparticles presented in this work may be a promising candidate for LIBs anode material.

ACKNOWLEDGEMENTS
The financial supports of the National Natural Science Foundation of China (61376002, 51503036), the Key Research Foundation for Young Scholars of Fujian Education Department of China (JZ160486, JZ160484), the Natural Science Foundation of Fujian Province (2017J01676, 2017J01677, 2017J01733, 2015J01654, 2015J05091, 2015J01632), and Fujian Education Deportment of China (JAT160558) are gratefully acknowledged.

References

1. W. D. Li, B. H. Song, A. Manthiram, *Chem. Soc. Rev*., 46 (2017) 3006.
2. J. Zhang, W. Zhang, T. He, I. S. Amiinu, Z. K. Kou, J. N. Li, S. C. Mu, *Carbon*, 115 (2017) 95.
3. B. Ahmed, D. H. Anjum, Y. Gogotsi, H. N. Alshareef, *Nano Energy*, 34 (2017) 249.
4. X. S. Zhou, L. Yu, X. W. Lou, *Adv. Energy Mater*., 6 (2016) 1600451.
5. R. Demir-Cakan, Y. S. Hu, M. Antonietti, J. Maier, M. M. Titirici, *Chem. Mater*., 20 (2008) 1227.
6. X. Ye, W. Zhang, Q. Liu, S. Wang, Y. Yang, H. Wei, *J. Phys. Chem*., 39 (2015) 130.
7. Y. D. Wang, T. Chen, *Electrochim. Acta*, 54 (2009) 3510.
8. Y. D. Wang, I. Djerdj, B. Smarsly, M. Antonietti, *Chem. Mater*., 21 (2009) 3202.
9. C. W. Wei, G. X. Zhang, Y. Bai, D. Yan, C. Y. Yu, N. Wan, W. F. Zhang, *Solid State Ion*., 272 (2015) 133.
10. X. K. Wang, Z. Q. Li, Z. W. Zhang, Q. Li, E. Y. Guo, C. X. Wang, L. W. Yin, *Nanoscale*, 7 (2015) 3604.
11. V. Subramanian, K. I. Gnanasekar, B. Rambabu, *Solid State Ion*., 175 (2004) 181.
12. H. W. Ha, K. Kim, M. De Borniol, T. Toupance, *J. Solid State Chem*., 179 (2006) 702.
13. L. P. Wang, Y. Leconte, Z.X. Feng, C. Wei, Y. Zhao, Q. Ma, W. Q. Xu, S. Bourrioux, P. Azais, M. Srinivasan, *Adv. Mater*., 29 (2017) 1603286.
14. K. N. Zhao, L. Zhang, R. Xia, Y. F. Dong, W. W. Xu, C. J. Niu, L. He, M. Y. Yan, L. B. Qu, L. Q. Mai, *Small*, 12 (2016) 588.
15. M. Joseph, H. Tabata, T. Kawai, *Jpn. J. Appl. Phys*., 38 (1999) L1205.
16. W. J. Dong, J. J. Xu, C. Wang, Y. Lu, X. Y. Liu, X. Wang, X. T. Yuan, Z. Wang, T. Q. Lin, M. L. Sui, I. W. Chen, F. Q. Huang, *Adv. Mater.*, 29 (2017) 1700136.
17. F. Fang, Y. Y. Zhang, X. Q. Wu, Q. Y. Shao, Z. H. Xie, *Mater. Res. Bull*., 68 (2015) 240.
18. J. Zhang, F. Huang, L. Zhang, *Nanoscale*, 2 (2010) 18.
19. Y. H. Cai, Y. H. Zhang, L. P. Ren, *J. Macromol. Sci*. B, 55 (2016) 547.
20. L. Xu, Y. Zhao, J. B. Lian, Y. G. Xu, J. Bao, J. X. Qiu, L. Xu, H. Xu, M. Q. Hua, H. M. Li, *Energy*, 123 (2017) 296.
21. S. H. Wei, R. Wu, J. K. Jian, F. J. Chen, Y. F. Sun, *Dalton Trans*., 44 (2015) 1534.
22. A. Das, V. Bonu, A. K. Prasad, D. Panda, S. Dhara, A. K. Tyagi, *J. Mater. Chem*. C, 2 (2014) 164.
23. F. Wang, Y. Han, C. S. Lim, Y. H. Lu, J. Wang, J. Xu, H. Y. Chen, C. Zhang, M. H. Hong, X. G. Liu, *Nature*, 463 (2010) 1061.
24. J. Zhang, X. H. Liu, S. H. Wu, M. J. Xu, X. Z. Guo, S. R. Wang, *J. Mater. Chem*., 20 (2010) 6453.
25. M. Kitano, K. Funatsu, M. Matsuoka, M. Ueshima, M. Anpo, *J. Phys. Chem*. B, 110 (2006) 25266.

26. M. R. Alenezi, A. S. Alshammari, K. D. G. I. Jayawardena, M. J. Beliatis, S. J. Henley, S. R. P. Silva, *J. Phys. Chem*. C, 117 (2013) 17850.
27. Y. J. Yang, Y. H. Wang, S. Yin, *Appl. Surf. Sci*., 420 (2017) 399.
28. H. D. Bian, Y. Y. Tian, C. Lee, M. F. Yuen, W. J. Zhang, Y. Y. Li, *ACS Appl. Mater. Interfaces*, 8 (2016) 28862.
29. Y. Liu, Y. Jiao, Z. L. Zhang, F. Y. Qu, A. Umar, X. Wu, *ACS Appl. Mater. Interfaces*, 6 (2014) 2174.
30. Y. J. Hong, M. Y. Son, Y. C. Kang, *Adv. Mater*., 25 (2013) 2279.
31. H. S. Oh, H. N. Nong, P. Straser, *Adv. Fun. Mater*., 25 (2015) 1074.
32. Y. Shimizu, A. Jono, T. Hyodo, M. Egashira, *Sensor Actuat. B-Chem*., 108 (2005) 56.
33. H. Guo, R. Mao, X. J. Yang, S. X. Wang, J. Chen, *J. Power Sources*, 219 (2012) 280.
34. W. Q. Hu, X. G. Yuan, X. L. Liu, Y. Guan, X. Wu, *J. Sol-Gel Sci. Techn*., 84 (2017) 316.
35. X. Y. Zhang, G. G. Xu, Z. W. Chen, H. Z. Cui, Z. H. Zhang, X. Y. Zhan, *Ceram. Inter*., 43 (2017) 4112.
36. Y. Q. Zhang, D. Li, L. G. Qin, P. L. Zhao, F. M. Liu, X. H. Chuai, P. Sun, X. S. Liang, Y. Gao, Y. F. Sun, *Sensor Actuat. B-Chem*., 255 (2018) 2944.
37. G. C. Xi, Y. T. He, Q. Zhang, H. Q. Xiao, X. Wang, C. Wang, *J. Phys. Chem*. C, 112 (2008) 11645.
38. C. P. Gu, W. M. Guan, X. S. Liu, L. L. Gao, L. Y. Wang, J. J. Shim, J. R. Huang, *J. Alloys and Compd.*, 692 (2017) 855.
39. M. H. Liu, H. C. Zhu, B. Wang, J. Cheng, W. P. Yan, S. F. Xia, Z. A. Tang, *Sensor Actuat. B-Chem.*, 232 (2016) 545.
40. F. H. Saboor, T. Ueda, K. Kamada, T. Hyodo, Y. Mortazavi, A. A. Khodadadi, Y. Shimizu, *Sensor Actuat. B-Chem*., 223 (2016) 429.
41. H. H. Niu, S. W. Zhang, R. B. Wang, Z. Q. Guo, X. Shang, W. Gan, S. X. Qin, L. Wan, J. Z. Xu, *J. Phys. Chem.* C, 118 (2014) 3504.
42. B. Mallesham, P. Sudarsanam, G. Raju, B. M. Reddy, *Green Chem*., 15 (2013) 478.
43. X. K. Wang, Z. Q. Li, Q. Li, C. B. Wang, A. L. Chen, Z. W. Zhang, R. H. Fan, L. W. Yin, *CrystEngComm*, 15 (2013) 3696.
44. P. Zhang, S. Y. Huang, B. N. Popov, *J. Electrochem. Soc*., 157 (2010) B1163.
45. Y. Jiang, T. Yuan, W. Sun, M. Yan, *ACS Appl. Mater. Interfaces*, 4 (2012) 6216.
46. M. Mohamedi, S. J. Lee, D. Takahashi, M. Nishizawa, T. Itoh, I. Uchida, *Electrochim. Acta*, 46 (2001) 1161.
47. S. H. Yu, D. J. Lee, M. Park, S. G. Kwon, H. S. Lee, A. Jin, K. S. Lee, J. E. Lee, M. H. Oh, K. Kang, Y. E. Sung, T. Hyeon, *J. Am. Chem. Soc*., 137 (2015) 11954.
48. R .S. Kalubarme, B. B. Kale, S. W. Gosavi, *Mater. Res. Express*, 4 (2017) 085026.
49. M. R. Smith, P. L. Johnson, D. Teeters, *Solid State Ion*., 225 (2012) 680.
50. Z. Wang, D. Luan, F. Y. C Boey, X. W. Lou, *J. Am. Chem. Soc*., 133 (2011) 4738.
51. D. Jiang, C. R. Wang, L. Sun, X. F. Xu, B. H. Wu, X. S. Chen, *Chem. Lett*., 46 (2017) 1639.
52. B. Zhao, Y. T. Xu, S. Y. Huang, K. Zhang, M. M. F. Yuen, J. B. Xu, X. Z. Fu, R. Sun, C. P. Wong, *Electrochim. Acta*, 202 (2016) 186.
53. Y. G. Wang, H. M. Liu, K. X. Wang, H. Eiji, Y. R. Wang, H. S. Zhou, *J. Mater. Chem*., 19 (2009) 6789.
54. C. Wang, Y. Zhou, M. Y. Ge, X. B. Xu, Z. L. Zhang, J. Z. Jiang, *J. Am. Chem. Soc*., 132 (2010) 46.
55. J. Li, J. Q. Guo, X. Zhang, R. F. Peng, *Ionics*, 22 (2016) 1.